

Parametric Model for the 3D Reconstruction of Individual Fovea Shape from OCT Data

Patrick Scheibe^{a,d}, Anfisa Lazareva^b, Ulf-Dietrich Braumann^{d,e}, Andreas Reichenbach^c,
Peter Wiedemann^b, Mike Francke^{a,c}, Franziska Georgia Rauscher^b

^a*Translational Centre of Regenerative Medicine (TRM), University Leipzig, Leipzig, Germany*

^b*Department of Ophthalmology, Leipzig University Hospital, Leipzig, Germany*

^c*Paul-Flechsig-Institute of Brain Research, Department of Pathophysiology of Neuroglia, University Leipzig, Leipzig, Germany*

^d*Interdisciplinary Centre for Bioinformatics, University Leipzig, Leipzig, Germany*

^e*Institute for Medical Informatics, Statistics, and Epidemiology (IMISE), University Leipzig, Leipzig, Germany*

Abstract

As revealed by *optical coherence tomography* (OCT), the shape of the fovea may vary greatly among individuals. However, none of the hitherto available mathematical descriptions comprehensively reproduces all individual characteristics such as foveal depth, slope, naso-temporal asymmetry, and others. Here, a novel mathematical approach is presented to obtain a very accurate model of the complete 3D foveal surface of an individual, by utilizing recent developments in OCT. For this purpose, a new formula was developed serving as a simple but very flexible way to represent a given fovea. An extensive description of the used model parameters, as well as, of the complete method of reconstructing a foveal surface from OCT data, is presented. Noteworthy, the formula analytically provides characteristic foveal parameters and thus allows for extensive quantification. The present approach was verified on 432 OCT scans and has proved to be able to capture the whole range of asymmetric foveal shapes with high accuracy (i.e. a mean fit error of 1.40 μm).

Keywords: Fovea Shape, Mathematical Model, 3D Reconstruction, Optical Coherence Tomography (OCT)

1. Introduction

In current ophthalmology, *optical coherence tomography* (OCT) is an accepted, useful, and valuable diagnostic tool for non-invasive, image-based retinal structure analysis (Geitzenauer et al., 2011). In recent years, several technological developments of the OCT have further improved the image quality (Podoleanu and Rosen, 2008). OCT is especially useful both to display foveal structures and to diagnose pathological changes of the macula region in various degenerative diseases, such as age dependent macula degeneration, macular hole, or macula edema. In addition to monitor pathological changes, high resolution OCT enables ophthalmologists to characterize foveal structure variants within the normal population.

The shape of the fovea has long been under investigation. Specifically, it has been suggested that the high visual acuity of predatory birds is related to their deep funnel-shaped fovea, magnifying the image at the level of the photoreceptor cells (Walls, 1942). Furthermore, it has been questioned whether in humans certain foveal shapes favor a predisposition of macular diseases and whether diseases influencing foveal shape and structure directly impair visual acuity (Barak et al., 2011).

*Corresponding author. Tel.: +49 341 97 39483; Fax.: +49 341 97 39609; Address: Translational Centre for Regenerative Medicine (TRM), University Leipzig, Philipp-Rosenthal-Straße 55, 04103 Leipzig
Email address: pscheibe@trm.uni-leipzig.de (Patrick Scheibe)

Recent investigations revealed a significant variability of the foveal shape and foveal pit morphology in the normal human population (Tick et al., 2011; Ooto et al., 2011). These demonstrated race- and sex-related differences in retinal thickness, pit morphology (Wagner-Schuman et al., 2011), and age dependent changes (Ooto et al., 2010, 2011) and showed a correlation of both the foveal shape characteristics and the size of the foveal avascular zone (Dubis et al., 2012). Several parameters of foveal morphology were used to evaluate characteristics of foveal structure, such as pit diameter, pit depth, slope of the pit walls, central foveal thickness, macular retinal thickness, or macular volume (Tick et al., 2011; Wu et al., 2008; Dubis et al., 2009; Barak et al., 2011).

To extract the aforementioned fovea features reliably and reproducibly, a mathematical model, which can be fitted onto different datasets, is highly desirable. By reducing the measured OCT data to a small set of model-parameters, the extraction of fovea characteristics can be broken down to the pure analysis of the model function.

There exist already several approaches to find such a mathematical description of the foveal pit. In early publications it was approximated by a Gaussian function (Williams, 1980). While this approach has some merits because of its pureness and simplicity, certainly, it cannot reflect all features required for an automated quantification of individual foveal pits. A more general method was presented by Dubis et al. (Dubis et al., 2009), who used a *Difference of Gaussians* to obtain a better representation.

However, these previous approaches used a symmetric formula to represent the fovea mathematically. Regarding the fact that there are clear differences between nasal and temporal *nerve fibre layers* (NFL), foveas are asymmetric; thus, a separate, individual treatment of various directions from the foveal center is required.

Additionally, regarding the wide range of foveal shapes, including specimens with broad bottom but steep rim occurring in some higher primates, or very narrow and steep foveas observable in birds, methods presently available cannot comprise those variations with acceptable accuracy.

Therefore, this work proposes a simple but very flexible model suited for a wide range of foveal shapes. The approach is stable in the presence of noise and other artifacts, and it does not require noise-reducing pre-processing steps, because the fitting procedure chooses the most likely shape, even in the presence of noise. The model provides a mathematical description of the foveal surface, which can be analyzed extensively; in particular, most calculations can be carried out *analytically*. This has the overall advantage that analytically derived properties give deeper insights than pure numerical calculations can offer. Additionally, as it will be shown, this new model involves four parameters, which influence the foveal shape in a very intuitive way. Furthermore, parameters have utmost decoupled effects, i.e. every parameter adjusts only one specific shape characteristic while leaving the others almost unchanged. This important aspect enables the experimentalists to grasp the individual features of foveal shapes merely by inspecting the model-parameters. In summary, the new method enables both a detailed fovea surface reconstruction and the assessment of important shape characteristics.

Finally, once the model-parameters of a fovea are determined, one does not have to work on the raw and large OCT-data again. Since foveal properties are defined in terms of the model function, a certain characteristic number can instantly be calculated.

2. Materials and Supplies

To assess the methods proposed in this work, OCT scans obtained on 230 healthy subjects (49.7% male, with a mean age of 43.7 ± 13.6 years (range 21 to 78)) were employed. The mean spherical equivalent of the best corrected subjective refraction resulted in -0.72 ± 2.10 diopters for the right eye and in -0.66 ± 2.09 diopters for the left eye with a mean best corrected visual acuity of -0.12 ± 0.08 LogMAR for either eye, respectively. The research followed the tenets of the Declaration of Helsinki for the use of human subjects.

All data sets were captured with the Spectralis OCT (Heidelberg Engineering, Heidelberg, Germany), where each volume scan consisted of 97 B-Scans (at 512 A-Scans/B-Scan), and every A-Scan consists of 496 samples. This represents scanned volumes of approximately $5.99 \text{ mm} \times 6.05 \text{ mm} \times 1.92 \text{ mm}$.

All computations were carried out with Wolfram *Mathematica*[®] version 9.0.1. To import the *inner limiting membrane* (ILM) and the *retinal pigment epithelium* (RPE) as segmentation data from the Heidelberg Spectralis OCT raw data format, a *Mathematica*[®] import package was developed, which provides such functionality.

3. Detailed Methods

In this section, the approach of representing foveal surface shapes in terms of a new model function is shown. In order to reproduce the approach of this work, the following steps are required, which are discussed in detail in this section.

- The OCT scans contain different layers of the retina. The distinct and prominent borderlines of the ILM and the RPE are used as input data, which are inherently extracted by the OCT device's software. The height difference between ILM and RPE represents the fovea surface, which is later reconstructed. With this approach, it is easily possible to get rid of a tilt in the scan introduced during the measurement and the curved shape of the eye.
- The center of the foveal pit, defined as the deepest point or the smallest height between the ILM and the RPE borderline, respectively, is extracted automatically and used as origin in an interpolation scheme, which provides a continuous representation of the foveal surface.
- To approximate this surface using the model introduced later in section 3.1, the interpolating function is used in a radial model fit. As depicted in figure 2, a circular region around the foveal center is divided into equiangular *supporting directions*, where each directional shape is approximated by the model function.
- To reconstruct the final fovea, a function is derived transforming the radial support shapes into a closed foveal surface in Cartesian coordinates.
- The calculation of important characteristic properties are given in the last step.

3.1. Model description

The origin of the introduced model is the second derivative of a Gaussian function, which was extended in order to serve as a flexible model for a wide range of foveal shapes. In the history of fovea quantification, the Gaussian clearly takes a prominent role (Dubis et al., 2009; Williams, 1980). Therefore, it was only natural to choose it as starting point and to develop existing ideas into a more sophisticated method.

The second derivative of a Gaussian function in r can be given as

$$\mathcal{G}(r) = \partial_{rr} \exp[-r^2/2] = r^2 \exp[-r^2/2] - \exp[-r^2/2] \quad (1)$$

and is depicted in figure 1.

This fundamental form already shows typical shape features required for real foveas, however, it is a symmetric formula, i. e. $\mathcal{G}(r) = \mathcal{G}(-r)$. Since the goal is to model foveas which are asymmetric, only the right half with $r \geq 0$ is used. Therefore, unlike fitting the entire foveal profile with one formula as done by others (Dubis et al., 2009), a *one-sided* model is used in a radial fashion around the center of the fovea. In this way, every fovea is represented by several circularly equidistant fits starting at the center and directed radially outwards (see figure 2). By using only one half to the model function, foveas are no longer required to be symmetric which, in turn, will provide a greater flexibility in order to represent different and possibly asymmetric foveal shapes.

To extend equation 1 into a flexible model, four parameters, namely μ, σ, γ and α are introduced. The final form of the radial model is given by

$$\mathcal{M}(r; \mu, \sigma, \gamma, \alpha) = \underbrace{\mu\sigma^2 r^\gamma \cdot \exp[-\mu r^\gamma]}_A + \underbrace{\alpha(1 - \exp[-\mu r^\gamma])}_B \quad (2)$$

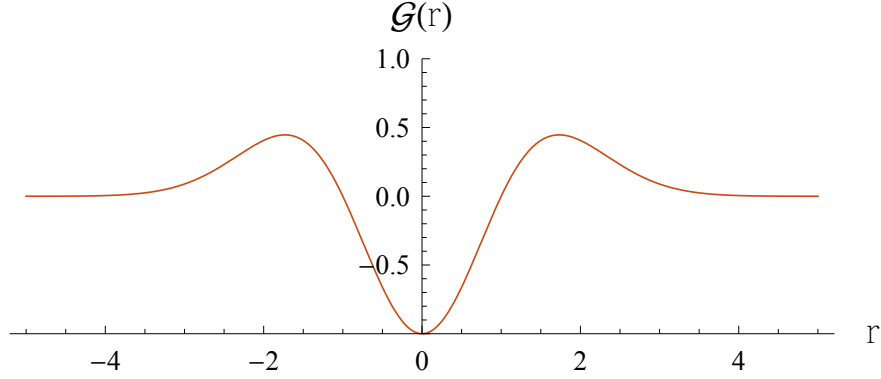


Figure 1: Second derivative $\mathcal{G}(r)$ of a Gaussian function (see equation 1) is the parameter-free fundamental form and shows already typical shape features of a fovea, e.g. the foveal pit as minimum in the center and a higher rim due to the thicker *nerve fiber layer* (NFL) around.

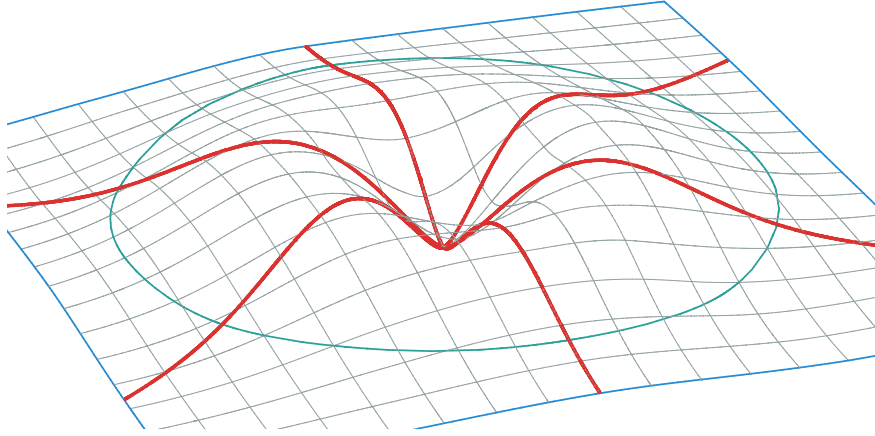


Figure 2: Foveal surface represented by *one-sided* fits of the presented model, which are equiangular distributed around the fovea center. Here, the red curves are individual model curves, where the final 3D surface is created by a special monotonic interpolation. The green circular line encloses the fit region defined by r_{\max} in equation 5 and therefore, everything outside this ring is an extrapolation.

Like the derivative of the Gaussian, equation 2 consists of two additive terms A and B , which are depicted separately in figure 3 to facilitate a deeper insight into the structure. Term A models the rim, an important feature appearing in many but not all foveas. Its height is proportional to the square of σ . Since this parameter does not appear in term B of \mathcal{M} , it has no influence on the shape of the fovea outside the rim region, which is modeled by term B .

The parameter α , only present in term B , controls the height of the monotonically increasing function in figure 3. Since beyond the rim a constant retinal thickness is assumed, the model function has to converge to a specific value. Therefore, α was introduced to influence term B in such a way that

$$\lim_{r \rightarrow \infty} \mathcal{M}(r; \mu, \sigma, \gamma, \alpha) = \alpha .$$

This states, while r approaches infinity and the function of term A is decreasing, the model converges to α . It can therefore be directly concluded that the retinal thickness outside the foveal center can be approximated by adding up α and the difference between ILM and RPE in the foveal center.

To steer the width of the foveal pit, another parameter μ was introduced. Unlike the mean in a Gaussian, where μ is an additive constant and therefore laterally shifts the whole function, here, μ instead is a factor of r inside the exponential. Therefore, it scales the function in r -direction, which also has the effect of shifting

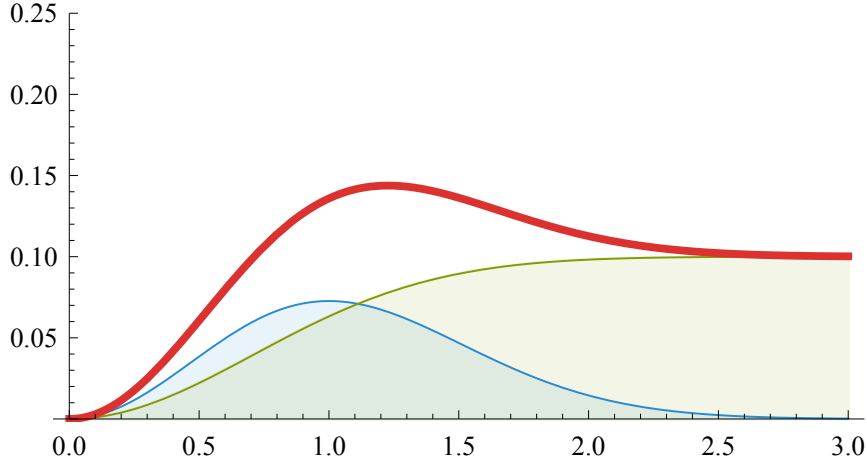


Figure 3: Additive terms of the model $\mathcal{M}(r)$ in blue and green and the resulting sum in red plotted against the radius r . The blue function depicts the term $A = \mu\sigma^2 r^\gamma \exp[-\mu r^\gamma]$. Term $B = \alpha(1 - \exp[-\mu r^\gamma])$ is shown in green.

the rim, but provides the important advantage of keeping the minimum of the foveal pit at $r = 0$, which is crucial for the approach.

Another occurrence of μ acts as factor in front of the term A in \mathcal{M} . It ensures that μ has no influence on the height of the rim. The property of having a constant rim height when changing μ can be shown by first calculating the maximum position r_{rim} as solution of

$$\partial_r \mathcal{M}(r; \mu, \sigma, \gamma, \alpha) = 0.$$

By solving this equation, the position of the rim maximum can be determined as

$$r_{\text{rim}} = \left(\frac{\alpha + \frac{\sigma^2}{\mu}}{\sigma^2} \right)^{\frac{1}{\gamma}}, \quad (3)$$

and it further can be shown that

$$\partial_\mu \mathcal{M}(r; \mu, \sigma, \gamma, \alpha)|_{r=r_{\text{rim}}} = 0,$$

which states that the height of the model at the point r_{rim} remains constant when μ changes.

The parameter γ is introduced as an exponent to r and serves to narrow or widen the rim and vice versa, to widening and narrowing the pit. The constraint $\gamma > 1$ needs to be fulfilled, thus, ensuring that the model has its minimum at $r = 0$. This can be shown by inspecting the first derivative of \mathcal{M} which is either infinite or indeterminate at $r = 0$ for $\gamma \leq 1$:

$$\partial_r \mathcal{M}(r; \mu, \sigma, \gamma, \alpha) = \alpha\gamma\mu \cdot r^{\gamma-1} \cdot \exp[-\mu r^\gamma] - \gamma\mu^2\sigma^2 \cdot r^{2\gamma-1} \cdot \exp[-\mu r^\gamma] + \gamma\mu\sigma^2 \cdot r^{\gamma-1} \cdot \exp[-\mu r^\gamma].$$

The vanishing derivative at the minimum ensures a smooth transition in the foveal center when several support shapes are later combined in the final 3D surface. Note that, by allowing γ to have non-integer values, the analyticity of the model function is reduced to the open ray $(0, \infty)$. For all practical purposes this does not play any role. In fact, the function is still differentiable at $r = 0$, if one defines it as $\lim_{r \rightarrow 0^+} \mathcal{M}'(r)$.

After this rather formal introduction of the model and its properties, the parameters' influence on the shape is illustrated by some specific examples. In figure 4(a), a shape curve is depicted for different values of μ . It shows that the larger its value the closer the rim appears to the fovea center. Simultaneously, for larger values the rim becomes more narrow, due to the fact that μ basically scales the whole curve. This implies that the steepness of the curve from the center to the rim top raises with larger values of μ . As

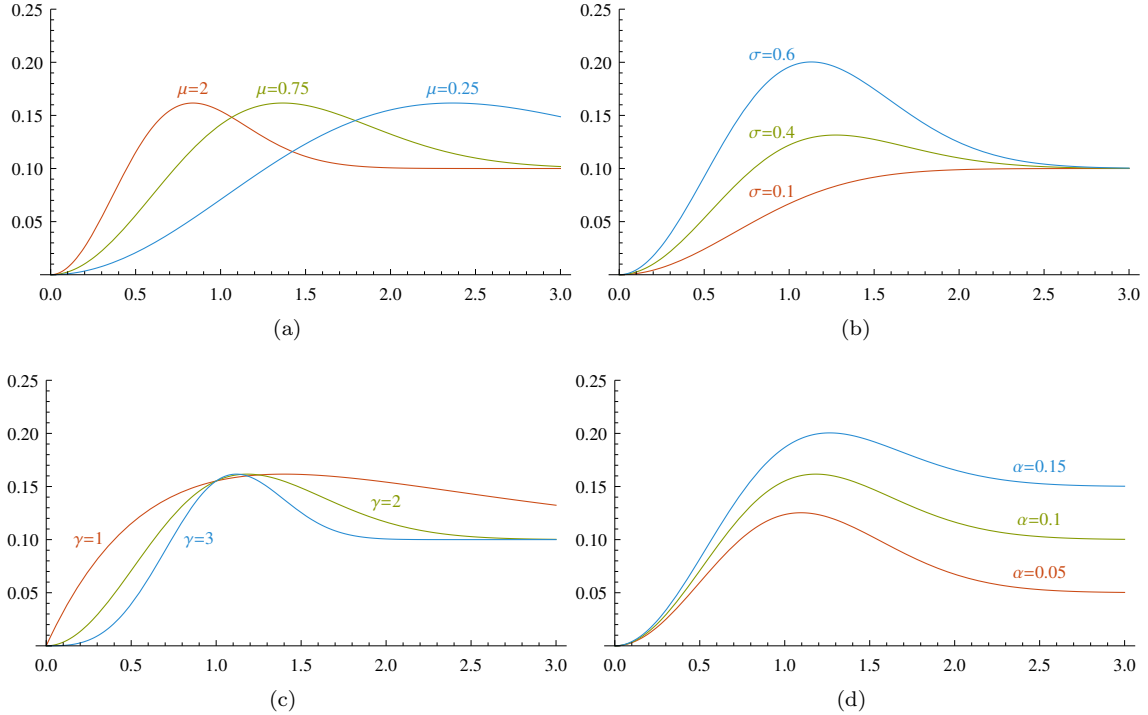


Figure 4: The model $\mathcal{M}(r; \mu, \sigma, \gamma, \alpha)$ plotted against the radius r to demonstrate the influence onto the shape, when different values for μ (a), for σ (b), for γ (c), and for α (d) are used. Unless labeled otherwise, the following values were used: $\mu = 1$, $\sigma = 1/2$, $\gamma = 2$, and $\alpha = 1/10$.

already mentioned, in the formal description it is important to note that μ does not change the height of the rim top.

Although α (since it globally changes the height) indirectly influences the rim height too, σ 's purpose in particular is to adjust the height of the rim component only. Figure 4(b) illustrates this influence of σ and shows that larger values increase the rim height.

The global influence of γ is depicted in figure 4(c). While values of $\gamma < 2$ produce a rather peaked foveal pit, values larger than two tend to widen the pit and create a peaked rim.

The purpose of α is to adjust the overall retinal thickness while leaving the foveal center unaffected. Figure 4(d) shows the model function for three different values of α .

3.2. Radial model fit

To capture the 3D surface of an OCT fovea data set, equation 2 is used as one-sided model to fit several directions radially from the center to the outside of a fovea. For this purpose, the center of the foveal pit was extracted from each data set by the following steps:

- Load ILM and RPE segmentation data from an exported Spectralis OCT data set. Each segmentation provides a height matrix of dimension $n_x \times n_y$. The dimension depends on the resolution setting of the OCT and was throughout this work 512×97 .
- Calculate the difference of RPE and ILM and filter the resulting matrix with a Gaussian filter. In this case an asymmetric filter with radius $r_1 = 5$ in x-direction and $r_2 = 2$ in y-direction was used, due to the sampling difference in the data set. This step is not crucial but prevents the following minimum search to get stuck in small local minima.

- Interpolate the data and search for a local minimum with starting point at $(n_x/2, n_y/2)$. The search was accomplished with the built-in function `FindMinimum` of *Mathematica*[®].

The automatically determined centers of the above approach were verified visually for every data set and have turned out to be exact down to the pixel in practically all cases.

In a next step, the difference between RPE and ILM is interpolated so that the constructed interpolation function $f_{\text{ip}}(x, y)$ has its origin in the previously calculated fovea center. Furthermore, the scaling factors of the OCT data are incorporated so that f_{ip} has metric dimensions. The interpolation is necessary since radial curves will in general not lie on the regular grid of the ILM/RPE segmentation data, but for the fitting procedure, a comparison between the model function and the underlying OCT data is required.

With such an interpolation function f_{ip} and the transformation to polar coordinates r and φ , the shape curves of the OCT data set (which are goal of the fit) instantly can be visualized. Figure 5 shows six angular directions of a foveal OCT scan, and it reveals two important characteristics of the fovea and the segmentation data: (i) there are indeed prominent shape variations between the different directions, and (ii) the shapes are affected with noise and other artifacts, e.g. vessels. The fitting procedure which follows will do both, it will find appropriate model parameter values for the different shapes and it will cope with the noise, without additional preprocessing steps.

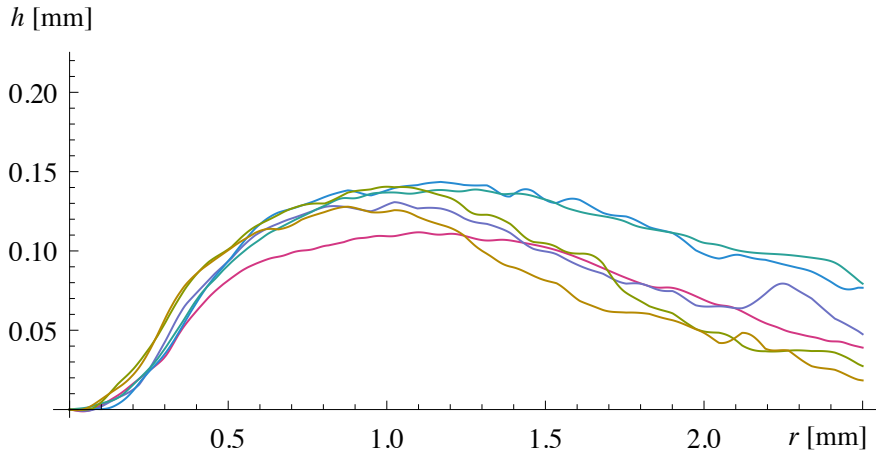


Figure 5: Here, $f_{\text{ip}}(r \cos(\varphi), r \sin(\varphi))$ is plotted against r for different φ , where f_{ip} is an interpolating function constructed from an OCT data set of one example subject. The angle φ was incremented by $\pi/3$. Note the occurring intra-subject shape variations for different directions.

The calculation of a parameter set for one direction firstly requires the definition of a certain distance function measuring the quality of the fit. For this purpose for one certain angle φ the integral over the squared errors was used:

$$\min_{\mu, \sigma, \gamma, \alpha} \int_0^{r_{\text{max}}} (f_{\text{ip}}(r \cos(\varphi), r \sin(\varphi)) - \mathcal{M}(r; \mu, \sigma, \gamma, \alpha))^2 dr \quad (4)$$

subject to $0 < \mu \leq 4$, $0 < \sigma < 2$, $1 < \gamma < 5$, $-1/2 < \alpha < 1/2$.

The constraints in equation 5 are a combination of the restrictions given in section 3.1 and practical experiences from a large number of successful model fits. While, theoretically, only $\mu > 0$ and $\gamma > 1$ are justified, the other bounds can help to speed up the minimization algorithm, which, if implemented, considers constrains in order to adjust search space.

To determine the solution of equation 5, a discretized version of the integral was used with the *Differential Evolution* optimization (Storn and Price, 1997), which is the underlying algorithm in *Mathematica*[®]'s `NMinimize` routine. This step is repeated to calculate a parameter set for every desired direction. At this

point it is worthwhile to note that the angle between each fitted direction is completely arbitrary, but smaller angles increase the number of directions, by this enhancing the resolution of the surface reconstruction. To give a specific example facilitating the understanding of the next section: The case which is displayed in figure 2 gives six parameter sets. The sampling directions which were fitted are $0, \pi/3, 2\pi/3, \dots, 5\pi/3$, where each fit is represented by separate values for μ, σ, γ , and α .

3.3. Fovea surface reconstruction

The calculated parameter sets from the previous subsections are further used to reconstruct the 3D surface of the foveal region. For this purpose, angular directions lacking a fitting parameter set are interpolated with a monotonic scheme (Steffen, 1990), which was adapted to be periodic to the first order derivative. For this, one only has to calculate the boundary derivatives by assuming that parameter values were padded periodically.

There are two reasons to use none of the usual interpolation schemes: Firstly, most interpolation methods tend to overshoot in several situations. Without additional fitting, it is basically unknown how the parameters behave in detail in between sampling directions. Therefore, it is a common serious assumption to make a smooth, monotonic transition between two values.

Secondly, in the fitted circular region, it is required that the angles $\varphi = 0$ and $\varphi = 2\pi$ have the same value and the same derivative. This provides equal smoothness on the 0-to- 2π -angle boundary as in the rest of the circular region.

This scheme is used to construct four interpolation functions, where each function represents the angle-dependent course for one parameter. To give an example: with n fitted directions the single $\mu_1, \mu_2, \dots, \mu_n$ are used to construct the following interpolation function:

$$\tilde{\mu}(\varphi) : [0, 2\pi] \mapsto \mathbb{R}.$$

With the model equation 2, the constructed interpolating functions $\tilde{\mu}, \tilde{\sigma}, \tilde{\gamma}$ and $\tilde{\alpha}$ and the transformation from polar to Cartesian coordinates, the final fovea surface can be given as

$$\mathcal{F}(x, y) = \tilde{\mu}(\varphi) \tilde{\sigma}(\varphi)^2 (x^2 + y^2)^{\tilde{\gamma}(\varphi)/2} \exp \left[-\tilde{\mu}(\varphi) (x^2 + y^2)^{\tilde{\gamma}(\varphi)/2} \right] + \tilde{\alpha}(\varphi) \left(1 - \exp \left[-\tilde{\mu}(\varphi) (x^2 + y^2)^{\tilde{\gamma}(\varphi)/2} \right] \right) \quad \text{with } \varphi = \text{atan2}(y, x) \quad (5)$$

Both figures 2 and 6 were created using the formula above. While the visualization of \mathcal{F} is surely very descriptive, the main application of the fovea reconstruction is the computation of characteristic property numbers as will be detailed in the following.

3.4. Characteristic properties

As said in the previous subsections, the computation of individual foveal characteristics is an even more important application of the model than visualization. In previous publications, some specific properties of the foveal shape were tried to be characterized and extracted from the OCT images. For example, central foveal thickness, foveal diameter, maximum slope or several symmetry measures can be found in various publications (Barak et al., 2011; Dubis et al., 2009).

Since the presented model has a simple form, it is possible to analytically calculate various properties, including the ones mentioned above, formally. Mathematically speaking, for the main properties this can be done without knowing numeric values for μ, σ, γ , and α .

For the one-sided model, as depicted in figure 3, important features are the following:

- the minimum at $r = 0$
- the first point of inflection between the minimum and the maximum at the top of the rim
- the maximum point at the top of the rim

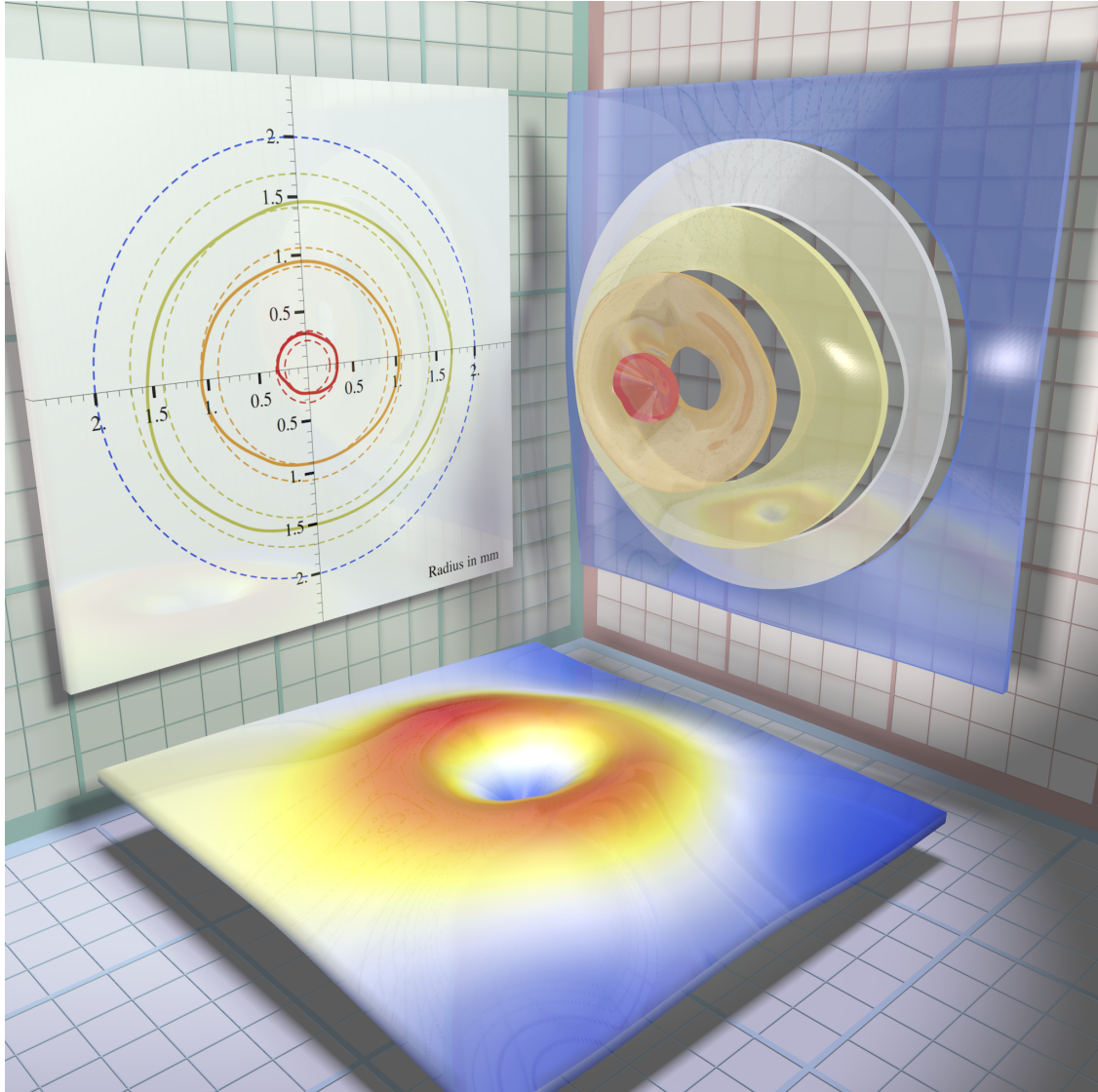


Figure 6: Visualization of a reconstructed foveal surface of a left eye. The three graphs correspond to each other in a way that the back left edge of the bottom surface is the top edge of both upper graphs (in the retina this corresponds to the superior position). In the bottom figure the full foveal surface with its different heights is illustrated. The upper right illustration is an exploded view, which shows the fovea as if it were cut along important characteristic points. These are from inside out: first inflection point, rim maximum line, second inflection point, and maximum fitting radius. The upper left part shows a projection of the foveal region boundaries, where it becomes visible that the different radii, in fact, are varying and the foveal structure is asymmetric. While in the bottom figure different heights are color-coded (red depicts the highest elevations), the top two figures utilize colors to separate different regions, whereby the coloring in left and right upper graphs correspond to each other. The front left part of the bottom surface corresponds to the nasal region of the fovea. This is clearly indicated by a higher elevation (coded in yellow) which is caused by thickening of the nerve fiber layer towards the optic nerve head. This is a general feature of retinal structure.

- the falling inflection point right to the top of the rim

The existence of the abovementioned points may depend on several conditions of the parameter values, e.g. $\gamma > 1$, as already mentioned. Those conditions were always met in the data sets processed.

To calculate the maximum point, the root of the first derivative of \mathcal{M} with respect to r has to be calculated. The solution of this was already given in equation 3. The radius r_{rim} can be used to calculate

a certain diameter for a fovea. Please note r_{rim} is varying over φ , caused by the asymmetric contour of the foveal shape, and, therefore, the definition of a single overall foveal diameter is not directly possible as is discussed later.

The two inflection points are the solution of $\partial_{rr}\mathcal{M} = 0$ and can be given as

$$r_{w_{1/2}} = 2^{\frac{-1}{\gamma}} \left(\frac{S_1 \pm S_2}{\gamma\mu^2\sigma^2} \right)^{\frac{1}{\gamma}} \quad \text{where} \quad (6)$$

$$S_1 = -\mu(-\alpha\gamma - 3\gamma\sigma^2 + \sigma^2) \quad \text{and}$$

$$S_2 = \mu\sqrt{\alpha^2\gamma^2 + 2\alpha\gamma^2\sigma^2 + 2\alpha\gamma\sigma^2 + 5\gamma^2\sigma^4 - 2\gamma\sigma^4 + \sigma^4}.$$

Figure 7 depicts some more model features, which are either directly accessible or can be calculated through the above approach. The value h_c is defined as the difference of RPE and ILM exactly at the center of the fovea, which was extracted automatically. Adding the value of the parameter α to h_c results in h_α , where it is important to note that α can be negative in cases where the depression of the foveal pit is not as deep as the retinal thickness in the perimacular area.

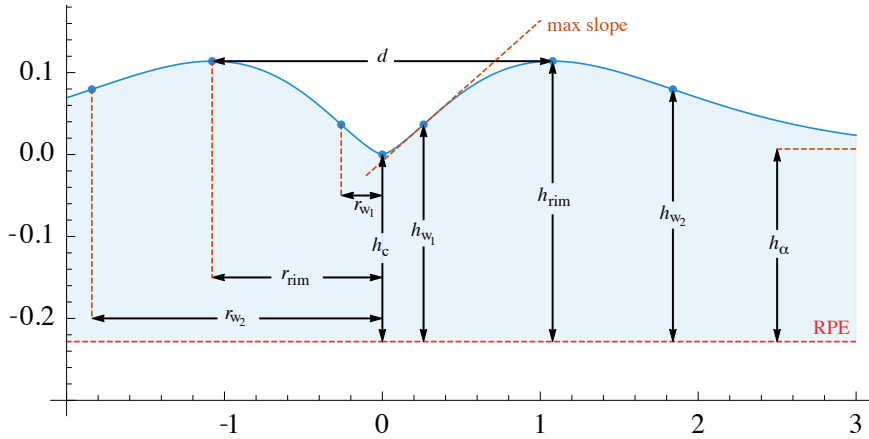


Figure 7: The model $\mathcal{M}(r; \mu, \sigma, \gamma, \alpha)$ plotted against the radius r with annotations of foveal properties, which can directly be computed from the model. Usually, the left and right side of a fovea are not symmetric, but to better depict all properties in one image, here the left side is a mirrored version of the right one. The origin of the coordinate system is at the center of the foveal bowl as described in section 3.2 and indicate distances in mm.

The other three heights h_{w_1} (point of maximal slope), h_{rim} (maximum retinal thickness at the rim), and h_{w_2} (point of maximal decreasing slope) can be calculated by adding h_c to $\mathcal{M}(r_{w_1})$, $\mathcal{M}(r_{\text{rim}})$, and $\mathcal{M}(r_{w_2})$, respectively.

The value d is the *foveal diameter*, which is often referred to in literature. Its value is given by the sum of both r_{rim} 's from opposite sides of the fovea, but always will depend on the direction φ and thus remains ambiguous.

The maximum slope line, which is drawn in the upper region of figure 7, can be calculated by evaluating $\partial_r\mathcal{M}$ at r_{w_1} . Since the formal expression of this is rather large and can easily be derived from previous formulas, it is not given here.

The ability to utilize characteristic fovea properties, for the whole circular region, is an important capacity of the presented method. This directly implies, e.g. unlike having only *one* maximum slope, this characteristic number can be given for each angle φ . This leads to several completely new quantification methods, which will be discussed in the following.

First, with the analysis of the model, it is possible to postulate novel analytic definitions of properties, which would be difficult to determine otherwise. For example, it is important to discuss whether a meaningful radius for the foveal region can be given, i.e. to define where the foveal region ends. Employment of the

given model could help to define such a radius, e.g. a fixed drop off of term A in equation 2 may be used as a meaningful boundary to define the foveal region. Exactly defined dimensions of the foveal region in an individual have advantages for comparative diagnostics. For instance, a calculation of pigmentation density in a defined foveal area, or its comparison to the foveal avascular zone, might be useful for a correlation with macular pathologies or developmental variations, respectively (Howells et al., 2011; Chui et al., 2012).

Another advantage of the model is that conventionally defined 2D fovea properties, such as maximum slope, are extended to 3D. This extension may lead to unexpected new insights as depicted in figure 6, in the projection shown on the upper left side. While the conventional 2D analysis results in the determination of a single *uniform* foveal diameter, it is clearly visible that such a uniform foveal diameter does not exist. In fact, feature points such as the maximum or the inflection points rather follow an ellipsoid curve, which can potentially be explained by the way of nerve fiber growth during embryogenesis (Steineke and Kirby, 1993).

This asymmetry of the fovea makes it also difficult to provide an exact measure of the volume inside the foveal bowl. In 2D models, the foveal *volume* is assessed from one cross-section area by integration. A re-calculation in 3D instantly reveals some problems: when both the radii of the foveal rim and its heights vary with the angle, the virtual upper limiting surface of the foveal bowl is not a simple plane. Therefore, a first step in defining a real foveal volume is to provide a meaningful definition of the upper limiting surface.

One beneficial aspect of the presented 3D reconstruction is that it opens a multitude of new opportunities to investigate the 3D characteristics of the foveal surface. Taking the radius of the foveal rim contour as example, it is now possible to investigate how much it deviates from a circular shape and to explore whether the asymmetries show particular patterns. Using the height of the rim contour, which varies along its path like a crest of the top of a mountain, it is crucial to verify the directional position of the maximal height (see upper left part of figure 6).

3.5. Results

From 460 OCT data sets available, 28 had to be dismissed, since either the quality of the scan or the RPE/ILM segmentation turned out to be insufficient. A detailed analysis of potential errors in the OCT acquisition is given in section 4. For the remaining 432 data sets, 12 directions (equally distributed in $\pi/6$ steps) were fitted with a fit radius of 2 mm each, and therefore exactly $432 \times 12 = 5184$ fits of the model were carried out.

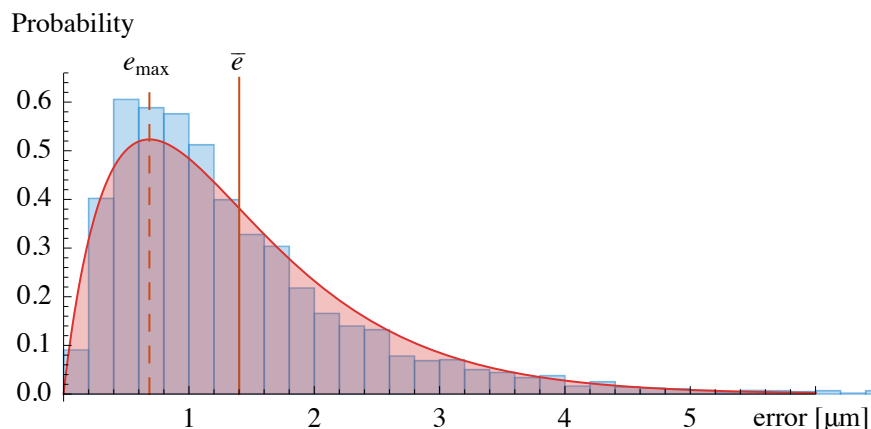


Figure 8: Histogram of the fitting errors. The errors are Gamma-distributed with a mean of $1.40 \mu\text{m}$. The maximum e_{max} of the distribution is at $0.684 \mu\text{m}$.

In figure 8 the distribution of the root mean square of all fits is depicted. The mean of this distribution is $1.40 \mu\text{m}$ with a standard deviation of $1.002 \mu\text{m}$. However, the mean retinal thickness of 230 subjects as measured by the Spectralis OCT was $231 \pm 19 \mu\text{m}$ for the right eye and $230 \pm 19 \mu\text{m}$ for the left eye (Center

Parameter	Mean	Standard deviation
μ	1.28	0.290
σ	0.471	0.0649
γ	1.69	0.243
α	0.0586	0.0452

Table 1: The mean and standard deviation of the model parameters found in 5184 fits.

Min, based on the minimum value within the central 1 mm circle), and therefore an error of 1.40 μm is negligible.

Table 1 shows statistical values of the parameters present in the model and describes the mean fovea shape of the population investigated. Note that, due to the distinct influence of each parameter on the profile of the model, the standard deviations cannot directly be compared.

4. Potential Pitfalls and Trouble Shooting

The most likely error source of the method is the OCT acquisition procedure, because most artifacts appearing are measurement inaccuracies, caused by the technician during the OCT scan acquisition. The following list provides detailed explanations of all errors, which were found in the collection of patient scans employed:

- During the measurement, the technician aims to keep the laser at the right distance to the retina. This adjustment has to be done manually and failed in 14 cases. The result is a horizontal cropping at the top of the scan, which appears as sharp cut-off in the final OCT scan.
- In an optimal measurement, the laser is centered in the pupil plane to maximize the light intensity reaching the retina. When the technician does not recenter the laser optimally, a vertical cropping of the scan occurs. The final OCT scan is affected by two artifacts: primarily, the scan appears slanted to one side, and, if not corrected at this point, a gradual fading towards the edge of the scan occurs. 7 data sets were affected by the second error.
- When the subject does not fixate centrally, the measured region has to be adjusted by the technician to map the foveal region of interest. If the technician fails to carry out this manual re-mapping, a different area of the retina is scanned, and the fovea is not centered in the final OCT data set. With a de-centered fovea, insufficient data is available in some directions, and the model fit cannot be carried out. This has occurred in 4 data sets.
- In subjects where the vitreous body is retracted a second bright line appears in the OCT scan, somewhat parallel to the retina. This line is falsely detected as ILM by the Spectralis OCT segmentation software, and renders a model fit impossible. This has occurred in 3 cases.

Another potential source of error is the retina layer detection algorithm of the Spectralis OCT on boundary regions. Although, the software extracted the layer data reliably for most parts of the scanned volume, near the boundary a few data points were missing in some of the examined patient scans. Therefore, one should include a safety margin instead of fitting the model for the whole extend of the scanned area to ensure that the procedure uses correctly identified RPE/ILM data only.

Although, the above errors are not related to the model procedure, they might have a severe impact on the overall success of the approach.

Another potential pitfall is the usage of the model for representing the retinal surface outside the fitted region. Figure 9 shows the central slice of a region extended beyond the modeled area. The red line depicts the model function with the calculated parameters for this specific fovea. Noteworthy, only the solid line represents the region fitted, while the dashed part shows a strikingly good accordance with the real retinal

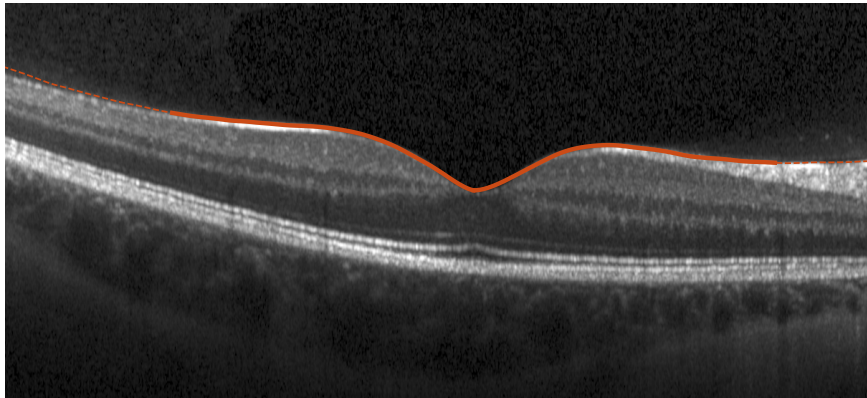


Figure 9: Back-projection of a reconstructed fovea of an individual subject into the appropriate image plane of the original data set. This specific OCT scan was 9 mm in x-direction, the fitted range was 5 mm. This image shows that the model outlines the data even outside the region for which the fit was obtained (dashed part). Note that y-to-x axis ratio of the reconstruction was adjusted to that of the OCT image.

surface even outside the modeled area. However, one should always be aware that areas outside the fitted regions are an *extrapolation* and should not be used without verification.

In summary, the newly developed model allows, for the first time, a detailed 3D analysis of the fovea, additionally to an exact mathematical calculation of all relevant parameters, which describe the foveal structure and its asymmetry. By applying this model, a few defined parameters can be used to compare individual foveal profiles. This information can, for instance, be correlated with visual performance of a patient or other diagnostic findings, including indications of certain macular diseases.

Acknowledgment

The first author is indebted to Jan Mangaldan for recommendations and extensive discussions about interpolation methods and for pointing him to the work of Steffen (Steffen, 1990).

The work presented in this paper was made possible by funding from the German Federal Ministry of Education and Research (BMBF 1315883) and from funding by the Deutsche Forschungsgemeinschaft (GRK 1097/1 and 1097/2 to AR).

References

- Barak, Y., Sherman, M.P., Schaal, S., 2011. Mathematical analysis of specific anatomic foveal configurations predisposing to the formation of macular holes. *Investigative Ophthalmology & Visual Science* 52, 8266–8270.
- Chui, T.Y., Zhong, Z., Song, H., Burns, S.A., 2012. Foveal avascular zone and its relationship to foveal pit shape. *Optometry & Vision Science* 89, 602.
- Dubis, A.M., Hansen, B.R., Cooper, R.F., Beringer, J., Dubra, A., Carroll, J., 2012. Relationship between the foveal avascular zone and foveal pit morphology. *Investigative Ophthalmology & Visual Science* 53, 1628–1636.
- Dubis, A.M., McAllister, J.T., Carroll, J., 2009. Reconstructing foveal pit morphology from optical coherence tomography imaging. *British Journal of Ophthalmology* 93, 1223–1227.
- Geitzenauer, W., Hitzenberger, C.K., Schmidt-Erfurth, U.M., 2011. Retinal optical coherence tomography: past, present and future perspectives. *British Journal of Ophthalmology* 95, 171–177.
- Howells, O., Eperjesi, F., Bartlett, H., 2011. Measuring macular pigment optical density in vivo: a review of techniques. *Graefe's archive for clinical and experimental ophthalmology* 249, 315–347.
- Ooto, S., Hangai, M., Sakamoto, A., Tomidokoro, A., Araie, M., Otani, T., Kishi, S., Matsushita, K., Maeda, N., Shirakashi, M., et al., 2010. Three-dimensional profile of macular retinal thickness in normal japanese eyes. *Investigative Ophthalmology & Visual Science* 51, 465–473.
- Ooto, S., Hangai, M., Tomidokoro, A., Saito, H., Araie, M., Otani, T., Kishi, S., Matsushita, K., Maeda, N., Shirakashi, M., et al., 2011. Effects of age, sex, and axial length on the three-dimensional profile of normal macular layer structures. *Investigative Ophthalmology & Visual Science* 52, 8769–8779.

- Podoleanu, A.G., Rosen, R.B., 2008. Combinations of techniques in imaging the retina with high resolution. *Progress In Retinal and Eye Research* 27, 464–499.
- Steffen, M., 1990. A simple method for monotonic interpolation in one dimension. *Astronomy and Astrophysics* 239, 443.
- Steineke, T.C., Kirby, M.A., 1993. Early axon outgrowth of retinal ganglion cells in the fetal rhesus macaque. *Developmental brain research* 74, 151–162.
- Storn, R., Price, K., 1997. Differential evolution – a simple and efficient heuristic for global optimization over continuous spaces. *Journal of Global Optimization* 11, 341–359.
- Tick, S., Rossant, F., Ghorbel, I., Gaudric, A., Sahel, J.A., Chaumet-Riffaud, P., Paques, M., 2011. Foveal shape and structure in a normal population. *Investigative Ophthalmology & Visual Science* 52, 5105–5110.
- Wagner-Schuman, M., Dubis, A.M., Nordgren, R.N., Lei, Y., Odell, D., Chiao, H., Weh, E., Fischer, W., Sulai, Y., Dubra, A., et al., 2011. Race- and sex-related differences in retinal thickness and foveal pit morphology. *Investigative Ophthalmology & Visual Science* 52, 625–634.
- Walls, G.L., 1942. *The vertebrate eye and its adaptive radiation*. Bloomfield Hills, Michigan, Cranbrook Institute of Science.
- Williams, D.R., 1980. Visual consequences of the foveal pit. *Investigative Ophthalmology & Visual Science* 19, 653–667.
- Wu, P.C., Chen, Y.J., Chen, C.H., Chen, Y.H., Shin, S.J., Yang, H.J., Kuo, H.K., 2008. Assessment of macular retinal thickness and volume in normal eyes and highly myopic eyes with third-generation optical coherence tomography. *Eye* 22, 551–555.